arXiv:2610.42009v1 [astro-ph.EP] 30 Oct 2026

An end-to-end CNN search for ultra-short-period planets in TESS: from the blend ceiling to the independent validation of TOI-6662 b

Juan Francisco Pagés Navarrete[1*]

[1*]Independent researcher, Málaga, Spain.

Corresponding author(s). E-mail(s): jfpages@gmail.com;

Abstract

We trained a convolutional neural network to detect ultra-short-period planets in TESS photometry, following the procedure now standard in the field: synthetic transits as positives, eclipsing binaries as negatives. Measured that way it reaches an area under the ROC curve of 0.97. Keeping the same model and the same planets, but replacing the negatives with false positives that the TESS Follow-up Observing Program has actually rejected, the area falls to 0.50 — the value of a random classifier. The conventional benchmark had been measuring a problem that does not exist.

The reason is physical, and it bounds what is possible. Of 145 such false positives examined at pixel level, 42% are blends: eclipses belonging to a neighbouring star, diluted into the target aperture. Their light curves are indistinguishable from shallow transits, capping the attainable area at $\mathbf{1 - f/2 = 0.79}$. Retraining on real false positives reaches $\mathbf{0.80 \pm 0.06}$, confirming the ceiling independently. No classifier reading a single-band light curve can do better.

A detector alone is the wrong instrument. We built CASCADE-USP, a pipeline chaining the network with difference-image centroid analysis, scene modelling with high-resolution imaging and the Gaia astrometric solution, supplying in sequence what the light curve lacks. Its output is a prioritisation, not a verdict: it records what evidence each candidate still needs. Only the classifier is domain-specific; the other stages apply to any transit candidate. Of 435 unresolved TESS candidates it isolates 20; 19 prove false positives, traced to causes invisible in TESS photometry. The twentieth is TOI-6662 b, an Earth-sized planet ($\mathbf{0.94 \pm 0.03\ R_\oplus}$) orbiting an M dwarf every 7.05 hours. Our validation, independent of a concurrent one, agrees with it in planetary parameters and classification, closing the CASCADE procedure with an external check.

1 Introduction

1.1 Ultra-short-period planets

The study of ultra-short-period planets opens with CoRoT-7b [1], the first transiting super-Earth with a measured radius, on a 0.854 d orbit around a G9 dwarf, and with Kepler-10b [2], the first rocky planet identified by *Kepler*. Both established the existence of a population of terrestrial planets on orbits of hours, subject to conditions without analogue in the Solar System.

Ultra-short-period planets (USPs), conventionally defined by an orbital period below one day [3], constitute a singular population. They orbit at distances of a few stellar radii, where they receive irradiations of hundreds to thousands of times the terrestrial value and experience temperatures sufficient to melt silicates on their dayside. They are, almost without exception, of terrestrial size or smaller: the radius distribution falls sharply above $\sim$2 $R_\oplus$, a consequence of any gaseous envelope being stripped by photoevaporation in this irradiation regime [4, 5]. Their proximity to the host further places them close to the tidal disruption limit, which imposes lower bounds on their density [6].

Their interest is twofold. They offer direct access to the composition of planetary cores stripped of atmosphere — GJ 367 b, with 0.72 $R_\oplus$ and an iron fraction comparable to that of Mercury, is the paradigmatic example [7] — and their high transit frequency makes them favourable targets for characterisation. Their occurrence rate peaks around low-mass stars [8], so that M dwarfs constitute the natural hunting ground. The population remains small: only around a dozen ultra-short-period rocky planets orbiting M dwarfs have both mass and radius determined [9].

1.2 Deep learning for transit detection

Identifying transits in photometric surveys is an imbalanced classification problem over data volumes that make exhaustive inspection unfeasible. Since the foundational work of Shallue and Vanderburg [10], convolutional networks have become the reference tool, with successive developments incorporating domain knowledge [11], adapting to TESS data [12–14], or attaining statistical validation capability [15–17]. In the ultra-short-period regime, the GPFC method combines hardware-accelerated phase folding with convolutional classification [18]. Recent developments have diversified both architectures and inputs, with transformer-based models applied to full-frame images [19] and classifiers incorporating background flux and centroid information [20].

The declared performance of these systems is remarkably high: AUC values of 0.988 [10], 0.999 [15] and 1.0 [16] punctuate the literature. These figures are obtained, for the most part, by evaluating against negative sets built from simulations or from curated eclipsing-binary catalogues.

1.3 The benchmarking problem

We argue that this evaluation practice measures a substantially easier problem than the operational one, and that the resulting figures do not predict performance on real data.

The concern is not new. Osborn et al. [13] warned explicitly that transferring a model trained on simulations to real data would not perform with equal accuracy, and the review of Huertas-Company and Lanusse [21] identifies the shift from the simulated to the observational domain as a potential source of catastrophic failure. In the machine-learning literature the phenomenon is characterised: Geirhos et al. [22] term it *shortcut learning*, decision rules that perform well on standard benchmarks but fail to transfer to more demanding conditions, a manifestation of the "Clever Hans" effect described by Lapuschkin et al. [23]. Systematic biases introduced by deep networks when annotating large astronomical catalogues have been described in general terms by Dhar and Shamir [24]. What has been missing is a direct quantification of the magnitude of that degradation, and an identification of its physical cause.

That cause, we anticipate, is the *blend*: genuine eclipses originating in a star other than the target and diluted within the photometric aperture. With a pixel scale of 21 arcsec [25], TESS apertures routinely contain flux from several sources, so that the contaminating signal is indistinguishable from a shallow transit in the flux time series. The information that would allow discrimination — the colour, the position of the source, the surrounding stellar field — does not reside in the light curve. Twicken et al. [26], describing the difference-image diagnostic of the Data Validation module, state the point directly: the technique exploits spatial information contained in the pixel data, information that is not available in photometric flux time series.

1.4 This work

We present the construction, honest characterisation and application of a convolutional detector for ultra-short-period planets in TESS, organised around three contributions.

First, methodological.

We quantify the performance overestimation inherent in conventional benchmarking. Through a factorial design that varies the positive and negative classes separately, we show that the AUC of our detector falls from 0.97 against catalogued binaries to 0.50 — the chance value — against the real false positives of the TESS Follow-up Observing Program, and that the degradation is attributable entirely to the nature of the negatives.

Second, physical.

We identify and measure the limit imposed by blends. Difference-image analysis of 145 real false positives establishes that 42% are blends, irresolvable from single-band photometry. The maximum-performance prediction derived from that fraction converges on the AUC attained after retraining with real negatives: two independent determinations placing the detector at the ceiling of the photometric domain.

Third, observational and practical.

We formalise the resulting procedure in **CASCADE-USP** (CNN-Assisted Sequential Centroid And Dilution Evaluation), a pipeline chaining photometric classification with difference-image centroid analysis and dilution evaluation through TRICERATOPS

[27] and high-angular-resolution contrast curves, the latter located and retrieved automatically from ExoFOP. Applied to 435 unresolved TOI candidates, CASCADE-USP recovers 20 objects after spatial filtering, of which we document 19 false positives individually by failure mode and statistically validate one: **TOI-6662 b** (TOI-6662.01), an Earth-sized planet ($0.94 \pm 0.03\,R_\oplus$) on a 7.05-hour orbit around an M dwarf. The same object has been validated by Collier et al. [28] in an automated TRICERATOPS analysis of 443 TESS candidates. The two analyses are independent[1] and reach the object by different routes; their agreement (Sect. 6.3) is the last step of the CASCADE procedure: an external check of the full pipeline on a real planet.

The design of CASCADE responds directly to the diagnosis of this work. Since a substantial fraction of false positives is irresolvable from the light curve, the pipeline does not pursue a better classifier but the systematic incorporation of the information channels that photometry does not contain. Each stage contributes one of them: source position through pixel-level analysis [26, 29], and the stellar field and unresolved companions through scenario modelling with TRICERATOPS [27] and speckle imaging [30]. We further introduce a fourth channel, independent of the preceding three: the Gaia DR3 astrometric solution quality [31], which flagged one false positive that no other channel detected. The output is not a verdict but a decision table which, for each candidate, additionally records *what information is missing for validation*, allowing observing time to be prioritised.

The code, datasets and intermediate results supporting this article are published to permit reproduction and reuse. The framework is independent of the period regime: only the classification stage is domain-specific, so that adaptation to other populations reduces to retraining the classifier.

The article is organised as follows. Sect. 2 describes the detector and documents a spurious shortcut learned during its development, which prefigures the central result. Sect. 3 quantifies the performance collapse against real false positives and diagnoses its cause. Sect. 4 presents the retraining and the convergence with the predicted ceiling. Sect. 5 describes the application to unresolved candidates and the false-positive taxonomy. Sect. 6 presents the validation and characterisation of TOI-6662 b and compares them with those of Collier et al. [28]. Sects. 7 and 8 discuss the implications and summarise the conclusions.

2 The detector

2.1 Architecture and input representation

The classifier is a one-dimensional convolutional neural network operating on the phase-folded light curve. The input consists of 256 phase bins, standardised to zero mean and unit variance, with the transit minimum cyclically shifted to the central bin.

The network comprises four successive convolutional blocks — with 16, 32, 64 and 64 channels, and kernels of size 5, 5, 3 and 3 respectively — each followed by batch normalisation [32] and ReLU activation; the first three additionally incorporate max pooling with factor 2. Adaptive average pooling reduces the representation to

[1] This manuscript was first submitted to *Experimental Astronomy* on 13 August 2026, before the public release of Collier et al. [28] (arXiv:2608.21560, 21 August 2026).

a 64-component vector, which feeds a dense classifier head of 64 units with dropout regularisation [$p = 0.3$; 33] and a sigmoid output. The model totals of order 5×10^4 adjustable parameters. The design follows the convolutional approach established for folded light-curve classification [10, 12].

2.2 Training on synthetic data

The training set comprises 2×10^5 synthetic curves balanced between positives and negatives. Positives are generated as trapezoidal profiles with variable depth, width and flat-bottom ratio, on Gaussian noise. Negatives combine four populations: synthetic eclipsing binaries (40%), sub-threshold transits (20%), sinusoidal stellar variability (12%) and pure noise (28%).

The use of synthetic sets for training is widespread in this domain: Osborn et al. [13] employed pixel-level simulations generated with Lilith, Zucker and Giryes [34] evaluated convolutional networks for shallow transit detection on simulated data, and the GPFC method trains on two million synthetic curves [18].

The generation of the synthetic eclipsing binaries proved to be the critical element of the design, for reasons set out below.

2.3 Generator evolution and diagnosis of a spurious shortcut

We document here three successive iterations of the negative generator, whose outcome constitutes the first indication of the problem developed systematically in Sect. 3.

First version (v1).

Negatives consisted mostly of noise and variability, without realistic eclipsing binaries. Evaluated on a set of 513 real objects, the detector reached an AUC of 0.80, with a recall of 52% at the cost of a 28% false-positive rate: excessively permissive, it admitted binaries readily.

Second version (v2).

Synthetic eclipsing binaries with pronounced V-shaped profiles (flat-bottom ratio between 0 and 0.4) and secondary eclipses were introduced. The synthetic AUC rose to 0.99, but behaviour on real data proved erratic: the recall fell below 25%, with confirmed ultra-short-period planets receiving null scores.

The diagnosis was made by comparing the morphological properties of rejected against accepted curves, and yielded a result contrary to the initial hypothesis (Fig. 1). The rejected objects did *not* display the physical hallmarks of a binary: their secondary eclipses were shallower (-0.12 against -1.61 for the accepted ones) and their out-of-eclipse modulation smaller (0.138 against 0.797). What did distinguish them was the sharpness of the primary transit: the rejected curves were markedly more peaked (V-shape index of 4.10 against 2.10).

The cause proved to be a generator artefact. By constructing the synthetic binaries systematically as narrow V shapes, we had given them a morphological marker that the classifier learned to exploit: *the network learned that "narrow, sharp V equals eclipsing binary" rather than the physically discriminating signature, which is the presence of*

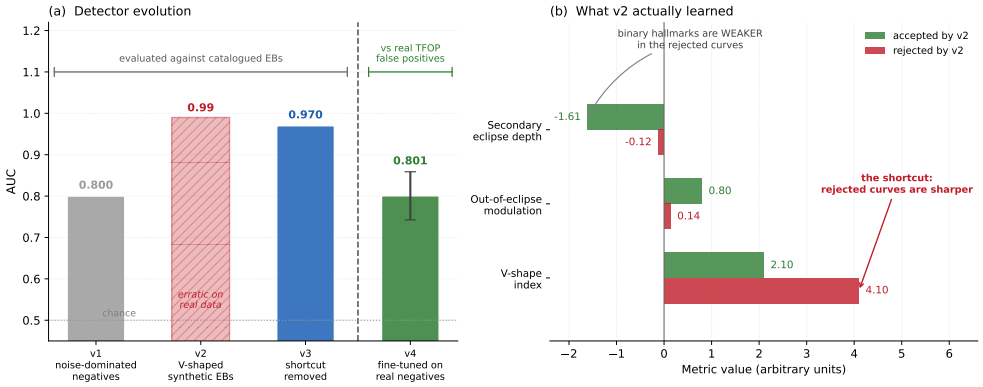


Fig. 1 Detector evolution and the geometric shortcut. Panel (a): AUC across the four versions. The vertical divider marks a change of evaluation set: v1–v3 are scored against catalogued eclipsing binaries, v4 against real TFOP false positives. The two benchmarks are not comparable — their non-comparability is the subject of Sect. 3 — and are separated for that reason. Version v2 attained a synthetic AUC of 0.99 while behaving erratically on real data. Panel (b): the morphological diagnostic that revealed the cause. Curves rejected by v2 display *weaker* binary hallmarks than those accepted — shallower secondary eclipses and smaller out-of-eclipse modulation — but are markedly sharper: the classifier had learned that a narrow, peaked transit indicates an eclipsing binary, a regularity of the generator rather than of the physics.

a secondary eclipse and ellipsoidal modulation — the standard diagnostics in binary classification [35]. The problem is that many real ultra-short-period planets produce, when folded, transits that are equally narrow and peaked, a consequence of the small number of cadences falling within the transit, so that they were classified as binaries.

The phenomenon corresponds to what Geirhos et al. [22] term *shortcut learning*: decision rules that perform satisfactorily on the usual evaluation sets but fail to transfer to more demanding conditions. It is a manifestation of the "Clever Hans" effect described by Lapuschkin et al. [23], in which a model attains high performance by exploiting a spurious correlation of the training set instead of the intended causal relation. In our case the spurious correlation was introduced inadvertently by the negative-generation procedure itself.

Third version (v3).

The correction consisted in deliberately removing the shortcut, making the synthetic binaries *indistinguishable from planets in primary-transit morphology*: the same width distribution, the same range of flat-bottom ratio, and overlapping depths. Binaries are then distinguished solely by the two features that physically separate them from a planet — the secondary eclipse at mid-phase and the ellipsoidal modulation — with each guaranteed to display at least one of them to avoid label noise.

Evaluated on the real set, v3 attains an AUC of 0.9699, with a recall of 93.6% against a 4.6% false-positive rate at the adopted decision threshold (0.02). It dominates both earlier versions: it recovers more planets than v1 with six times fewer false positives, and triples the recall of v2.

2.4 An irreducible false negative

One confirmed ultra-short-period planet, TOI-141 b [HD 213885 b; 36], receives a null score from all three versions of the detector, including the corrected one. The persistence of the failure after removing the geometric shortcut indicates that its cause does not lie in the generator.

The properties of the system suggest an explanation. TOI-141 b is a super-Earth of $1.74\,R_\oplus$ on a 1.008 d orbit around a bright G dwarf ($V = 7.9$), a configuration atypical relative to the dominant population of the training and validation sets — Earth-sized planets around M and K dwarfs. Its period further lies at the upper limit of the ultra-short-period definition, and the radius ratio against a solar-type host produces a shallow transit ($\sim$250 ppm) on a star whose brightness introduces its own instrumental systematics. The combination places this object in a region of parameter space sparsely represented during training.

We report this case as a known limitation: a confirmed object that the method systematically rejects, and whose recovery would require broadening the diversity of the training population towards solar-type hosts.

2.5 Foreshadowing

It is worth noting what this sequence reveals, because it prefigures the central result of this work. Version v2 attained a synthetic AUC of 0.99 while its operational performance collapsed, and the cause was that the classifier had learned a regularity of the generation procedure rather than the physics of the problem. *An excellent evaluation metric coexisted with a useless detector.* Geirhos et al. [22] note that detecting shortcuts requires evaluating under conditions different from those of training. The following section applies that principle systematically, with a considerably more severe result.

3 Performance against real false positives

3.1 The benchmarking problem

The standard evaluation of a deep-learning transit classifier measures its ability to separate planetary signals from false positives, using test sets built from synthetic light curves or curated eclipsing-binary catalogues (Sect. 1.2). Following this methodology, our v3 detector attains an AUC of 0.97 when discriminating confirmed USPs from the eclipsing binaries of Prša et al. [35], a catalogue of 4584 systems identified in sectors 1–26 from two-minute cadence photometry.

We argue that this figure measures a substantially easier problem than the operational one. The reason is twofold.

First, the nature of the negatives. Catalogued eclipsing binaries constitute a curated and morphologically distinctive population: they frequently display secondary eclipses, ellipsoidal variation, V-shaped profiles, or eclipse depths orders of magnitude larger than a planetary transit. A convolutional classifier learns to exploit these features readily. The false positives that actually contaminate a TESS transit search are of a different and considerably more adverse nature, dominated by *blends* — genuine

eclipses originating in a source other than the target and diluted within the photometric aperture — together with neighbour contamination, short-period stellar variability, and residual instrumental systematics.

Second, and critically for TESS, the spatial resolution. The TESS pixel scale is 21 arcsec [25], against ∼4 arcsec for *Kepler*. This difference, exceeding a factor of five in linear scale and hence twenty-five in area, implies a far higher density of contaminating sources per aperture. Tey et al. [14] attribute the poorer performance of these classifiers on TESS relative to *Kepler* precisely to larger pixels, higher false-positive rates, and shorter observational baselines. A performance figure obtained on *Kepler* — where blending is comparatively benign — does not transfer, and validation against synthetic EBs does not capture this population at all.

3.2 A representative test set

To quantify performance against the real population of contaminants we constructed an independent test set from the TESS Objects of Interest catalogue [TOI; 37].

The property that makes this catalogue suitable is not its size but its provenance. Threshold-crossing events identified by the SPOC [38] and QLP [39] pipelines are examined by the TESS Science Office before receiving a TOI designation, and events attributable to eclipsing binaries, variable stars, instrumental systematics or non-planetary transients are excluded from the TOI catalogue and archived separately. Consequently, TOIs subsequently labelled as false positives *are not morphologically obvious eclipsing binaries* — those were discarded before designation — but signals that passed both automated filtering and human vetting as plausible planetary candidates, and whose non-planetary nature was established only through photometric, spectroscopic or high-angular-resolution follow-up. They constitute precisely the population of difficult contaminants that a detector must learn to reject in operation, and that no eclipsing-binary catalogue represents.

We selected all TOIs with catalogued orbital period $P < 1.5$ d, obtaining 954 objects. This window is wider than the conventional definition of the ultra-short-period regime, $P < 1$ d [3], and the choice deserves justification.

First, the one-day cut-off is not astrophysically motivated: as Pu and Lai [40] note, it was adopted historically because planets known below that period were rare at the time, not because it marks a physical transition. Second, the occurrence rate is discontinuous in its neighbourhood, with an excess of planets immediately below the cut and appreciably different slopes of the period distribution on either side [41]. Third, and most relevant here, the migration pathways proposed for the formation of ultra-short-period planets source them from just above that boundary: from orbital periods of ∼1–3 d in the moderate-eccentricity scenario of Pu and Lai [40], and ∼1–5 d in the obliquity-driven tidal runaway of Millholland and Spalding [42]. The interval between 1 and 1.5 d is therefore physically continuous with the population of interest rather than external to it, and truncating the search exactly at one day would sever a transition region. The planet validated here has $P = 0.294$ d, comfortably within the ultra-short-period regime in the strict sense. We adopted as ground truth the disposition assigned by the TESS Follow-up Observing Program (TFOP) Working Group:

Table 1 Samples used in this work. The first two are evaluation sets built from different sources; the third is the application set, disjoint from the others by construction.

Sample	Composition	Size	Used for
Catalogue benchmark	confirmed USPs (positives) Prša EBs (negatives)	250 263	conventional evaluation (Sect. 3.3)
TFOP benchmark	TOI CP/KP (positives) TOI FP/FA (negatives)	111 253	realistic evaluation and retraining (Sects. 3.3, 4)
Blend subsample	TOI FP/FA with pixel data	145	measuring the blend fraction (Sect. 3.4)
Application set	TOI PC/APC, no ground truth	435	the search itself (Sect. 5)

- **Positive class** — *Confirmed Planet* (CP) and *Known Planet* (KP): planets confirmed by independent follow-up. After requiring SPOC two-minute cadence photometry, $N = 111$.
- **Negative class** — *False Positive* (FP) and *False Alarm* (FA): objects rejected by TFOP follow-up. Under the same requirement, $N = 253$.

We deliberately excluded the *Planet Candidate* (PC) and *Ambiguous Planet Candidate* (APC) dispositions, which by definition lack ground truth. These objects take no part in the evaluation and are reserved as the application set of Sect. 5.

We downloaded PDCSAP light curves [43, 44] at two-minute cadence, processed by the SPOC pipeline, from the Mikulski Archive for Space Telescopes using `lightkurve` [45]. Each curve was phase-folded at the catalogued period, rebinned to 256 points, standardised, and cyclically shifted to place the transit minimum at bin 128. This procedure is identical to that applied to the synthetic training set, so that any degradation observed is attributable to the nature of the data and not to a preprocessing mismatch.

Because several distinct samples appear in what follows, we summarise them in Table 1. Two are used for evaluation, one for retraining, one for the blend measurement and one for the search itself; they should not be confused with one another.

We acknowledge three limitations. First, the positive class carries a selection bias towards bright objects with deep transits, easier to confirm through radial velocities. Second, the classes are imbalanced (111 against 253), which is why we adopt the AUC as the primary metric, being invariant to class proportions. Third, the TFOP disposition, although the community standard, reflects the state of follow-up at the time of query.

3.3 The performance collapse

The v3 detector was initially evaluated on 250 confirmed ultra-short-period planets against 263 eclipsing binaries from Prša et al. [35], yielding an AUC of 0.97. Evaluated on the set described above, the value falls to 0.61. Since the two sets differ simultaneously in their positive and negative classes, this comparison alone does not attribute the degradation to either cause. To isolate the responsible variable, we evaluated the same model, without any retraining, on all four combinations of the two positive and

Table 2 Factorial evaluation of the v3 detector. The same model, without retraining, is evaluated on all four combinations of positive and negative classes.

Positives	Negatives	AUC	95% CI
Confirmed USPs (250)	Prša EBs (263)	0.9699	[0.951, 0.985]
Confirmed USPs (250)	TFOP FP/FA (253)	**0.5001**	[0.446, 0.549]
TOI CP/KP (111)	Prša EBs (263)	0.9761	[0.960, 0.989]
TOI CP/KP (111)	TFOP FP/FA (253)	0.6120	[0.553, 0.668]

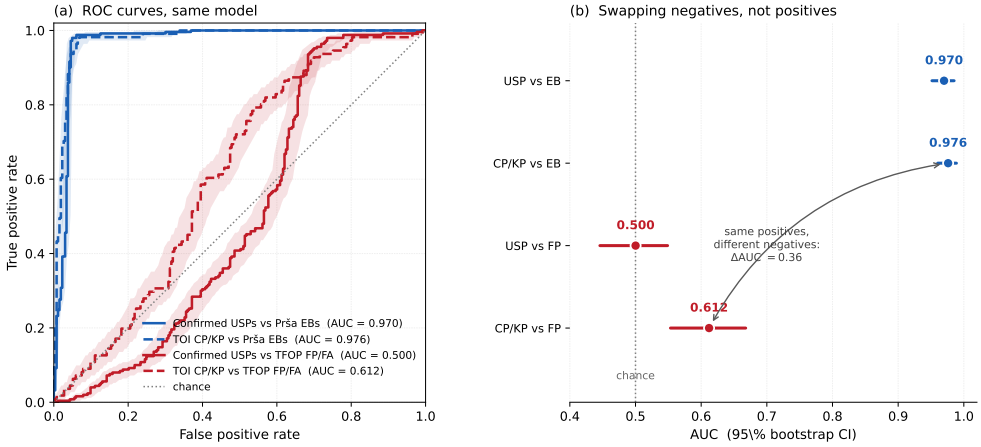


Fig. 2 The performance collapse. Panel (a): ROC curves for the same v3 model evaluated on all four combinations of two positive and two negative classes, with 68% bootstrap confidence bands. Colour encodes the negative class: blue for catalogued eclipsing binaries [35], red for real TFOP false positives. Panel (b): corresponding AUC values with 95% bootstrap confidence intervals. Holding the positive class fixed and substituting the negatives drives the AUC from 0.97 to chance, while substituting the positives leaves it essentially unchanged.

two negative classes (Fig. 2). Confidence intervals at the 95% level were obtained by stratified bootstrap with 2000 resamples.

The reading by rows and columns is unambiguous. Holding the negative class fixed, substituting one positive class for the other alters the AUC by 0.006 (0.9699 → 0.9761) against the Prša EBs and by 0.112 against the TFOP false positives; in the first case the difference is negligible and in both the confidence intervals overlap widely. Holding the positive class fixed, by contrast, substituting catalogued eclipsing binaries for real TFOP false positives drives the AUC from 0.9699 to 0.5001, with disjoint confidence intervals separated by more than four tenths.

The degradation is attributable almost entirely to the nature of the negative class, and not to that of the positive class.

The value of 0.5001 deserves emphasis: it is that of a random classifier, and its confidence interval contains 0.5. Faced with the false positives that actually contaminate a TESS transit search, the v3 detector — the same that attains 0.97 on the conventional benchmark — possesses no discriminating power whatsoever.

All 877 light curves used in the four experiments were downloaded from MAST with `lightkurve`, selecting exclusively SPOC-processed PDCSAP photometry at 120 s cadence, and subjected to the same procedure. The observed degradation cannot therefore be attributed to differences in instrumental provenance or preprocessing.

We state explicitly that the two positive classes are not independent: 109 of the 111 TOIs with CP/KP disposition also appear among the 250 confirmed USPs of the original set. Far from weakening the conclusion, this reinforces it: with essentially nested positive classes, the variation observed on changing only the negative class admits no alternative explanation in terms of sample composition.

3.4 The irreducible blend fraction

To identify the origin of the failure we applied a difference-image analysis [26, 29] to a sample of the TFOP false positives. We downloaded the target pixel files of each object (SPOC, 120 s cadence) and constructed the difference image by subtracting the median of the in-transit frames from the median of the out-of-transit frames, adopting a half-width of 0.05 in phase as the in-transit interval. The resulting image contains only the flux that disappears during the eclipse; its flux-weighted centroid locates the source of the signal. We compared that position with the centroid of the target measured on the out-of-transit image, and classified as a blend any case with an offset exceeding 1.0 pixel.

We adopted an absolute threshold rather than a criterion of statistical significance. In preliminary tests, a 3σ criterion erroneously classified as blends confirmed planets with offsets of barely 0.4 pixels, since the centroid uncertainty is small when the signal is deep.

We verified the test bidirectionally on a control sample of confirmed ultra-short-period planets: five of six show offsets below 1.0 pixel and are correctly classified as on-target, with offsets between 0.38 and 0.98 pixels. The single failure (1.066 pixels) lies marginally above the threshold.

We applied the test in two stages. A pilot sample of 30 objects was analysed first, of which 27 had usable target pixel files and 12 showed a displaced source. A second, larger pass drew 150 further objects, of which 118 had usable pixel files and 49 showed a displaced source; the remaining 32 lacked two-minute aperture photometry. Combining the two passes, **61 of 145 analysed false positives (42.1%; 95% Wilson confidence interval [34.3%, 50.2%]) are blends** (Fig. 3). These counts refer to false positives drawn from the TFOP benchmark of Table 1, and should not be confused with the 250 confirmed planets that form the positive class of the catalogue benchmark.

For these objects the light curve extracted from the target aperture is, by construction, indistinguishable from that of a shallow planetary transit. The information that would allow correct classification — the position of the source — resides in the pixel data, not in the flux time series. As Twicken et al. [26] state in describing this

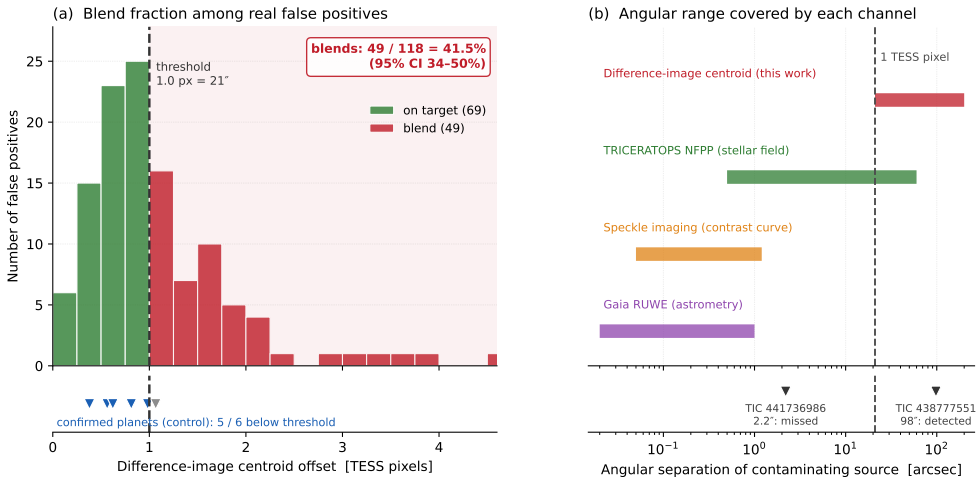


Fig. 3 The blend fraction and the reach of each vetting channel. Panel (a): distribution of difference-image centroid offsets for real TFOP false positives; the dashed line marks the 1.0-pixel decision threshold, and the markers below show the confirmed ultra-short-period planets used as a control sample, five of six falling below it. Panel (b): the range of angular separations over which each channel is sensitive to a contaminating source. The centroid test reaches only beyond one TESS pixel, which is why the measured blend fraction is a lower bound: the contaminant of TIC 441736986, at 2.2″, is missed, while that of TIC 438777551, at 98″, is detected.

same diagnostic, the technique exploits spatial information contained in the pixel data, information that is not available in photometric flux time series. Consequently, *no classifier operating on the folded light curve can resolve this fraction*, irrespective of its architecture or training set.

This fraction is a lower bound, for two reasons. First, the 1.0-pixel threshold corresponds to 21 arcsec [25]; blends produced by neighbours at smaller separations — predominant given the TESS pixel scale — are not detectable by this procedure. By way of contrast, the *Kepler* Robovetter operates with thresholds of 1–2 arcsec on pixel-response-function fits. Second, 32 of the 150 selected objects lacked two-minute aperture photometry and were excluded; these derive mostly from faint-star searches in full-frame images, and may be expected to show a higher, not lower, incidence of blends.

4 Retraining with real false positives

4.1 Rationale

The analysis of Sect. 3.4 establishes that approximately 42% of real false positives are blends, physically irresolvable from the light curve. The complementary implication is that the remaining fraction — around 58% — carries signatures that do reside in the photometry and are therefore learnable. The collapse documented in Sect. 3.3 is not due solely to a physical limit: it also reflects that the detector was never exposed during training to this class of contaminant.

Given the size of the available set (364 curves), training from scratch would lead to overfitting. We adopt instead a fine-tuning procedure: we start from the v3 weights — which already encode transit morphology, learned from 2×10^5 synthetic curves — and readjust the decision boundary with real data.

This procedure has established precedents in astronomy. Domínguez Sánchez et al. [46] pre-trained a convolutional network on SDSS galaxy morphologies and fine-tuned it to DES imaging, showing that the number of labelled examples required is reduced by a factor of a few relative to training from scratch; equivalent strategies have been employed between other survey pairs [47, 48], and Walmsley et al. [49] have shown that representations learned by solving a broad set of morphological tasks substantially improve performance on new tasks. Our case shares the same structure — an abundant source of pre-training examples and a scarce target set — with the difference that the source domain is synthetic rather than observational, which aggravates the distribution shift documented in Sect. 3.

The direction of transfer conditions the outcome: Tang et al. [48] observed that inheriting weights pre-trained on high-resolution imagery improves performance when fine-tuning on lower-resolution data, whereas transfer in the opposite direction degrades the classifier. Our case corresponds to the less favourable direction — from a synthetic domain, cleaner and of lower complexity, to an observational one — which makes the improvement obtained the more notable.

4.2 Training set and protocol

We use the set described in Sect. 3.2: 111 TOIs with CP/KP disposition as positives and 253 with FP/FA disposition as negatives, with identical photometry and preprocessing. The PC and APC candidates are excluded by construction, which guarantees that the application set of Sect. 5 is disjoint from the training set.

Fine-tuning is performed with the Adam optimiser [50, learning rate 3×10^{-4}, weight decay 10^{-4}], batches of 32 samples and 40 epochs, minimising binary cross-entropy with positive-class weighting $w = 253/111 = 2.28$ to compensate the imbalance. The architecture is inherited unmodified from v3. The learning rate is deliberately set low: the aim is to readjust the decision boundary without destroying the representations learned on the synthetic set.

Evaluation protocol.

We adopt nested stratified five-fold cross-validation. In each fold, 80% of the data constitutes the fitting set and the remaining 20% the test set. The fitting set is in turn subdivided (80/20, stratified) into training and inner validation; the stopping epoch is selected by performance on the inner validation set, and the test fold is evaluated *once only*, with the weights so selected.

This nesting is not an optional precaution. Varma and Simon [51] demonstrated that using the same cross-validation loop to select the model and to estimate its performance introduces an optimistic bias whose magnitude grows as the ratio of samples to parameters decreases, and Cawley and Talbot [52] showed that this bias additionally favours unnecessarily complex models; both works recommend nested cross-validation as the remedy. Our set lies precisely in the regime where these authors

Table 3 Fold-by-fold cross-validation results. The nested protocol selects the stopping epoch on an inner validation split and evaluates the test fold once; the non-nested protocol selects it on the test fold itself.

Fold	v3	v4 (nested)	v4 (non-nested)
1	0.6649	0.8966	0.9020
2	0.4813	0.7201	0.7807
3	0.6114	0.7718	0.8226
4	0.6791	0.8200	0.8800
5	0.6209	0.7945	0.8182
Mean	0.6115 ± 0.0700	$\mathbf{0.8006 \pm 0.0582}$	0.8407 ± 0.0441

predict the strongest effect: 364 samples against of order 5×10^4 adjustable parameters. We quantify the bias by running both protocols on the same folds.

4.3 Results

Fine-tuning with real negatives raises the AUC from 0.6115 to 0.8006 ± 0.0582, an improvement of +0.189 consistent across all five folds (range +0.055 to +0.239). The resulting model is designated v4.

The non-nested protocol yields 0.8407, that is, 0.040 above the value obtained with nesting. The magnitude of the effect agrees with the qualitative prediction of Varma and Simon [51] for small sets, and is comparable to the differences customarily invoked to establish the superiority of one architecture over another. We report it explicitly because it illustrates, on our own work, the same class of overestimation through deficient evaluation that motivates this article.

4.4 The ceiling imposed by the blend fraction

The value attained admits a quantitative interpretation in terms of the independent measurement of Sect. 3.4.

The area under the ROC curve admits the interpretation, established by Hanley and McNeil [53], of the probability that a randomly chosen positive receives a higher score than a randomly chosen negative — a quantity equivalent to the non-parametric Wilcoxon statistic. Let f be the fraction of negatives that are blends. Under the assumption that these are statistically indistinguishable from positives in the photometric domain — so that for such pairs the probability is 0.5 — and of perfect separability over the remainder, the maximum attainable AUC is

$$\mathrm{AUC}_{\max} = (1 - f) \cdot 1 + f \cdot 0.5 = 1 - f/2. \tag{1}$$

Substituting the fraction measured in Sect. 3.4, $f = 0.421$, gives $\mathrm{AUC}_{\max} = 0.789$. Propagating the confidence interval on f ([0.343, 0.502]) gives a predicted ceiling in the range [0.749, 0.829].

The measured value, 0.8006 ± 0.0582, lies within that interval and 0.19σ from the central prediction (Fig. 4). *Two methodologically independent determinations* —

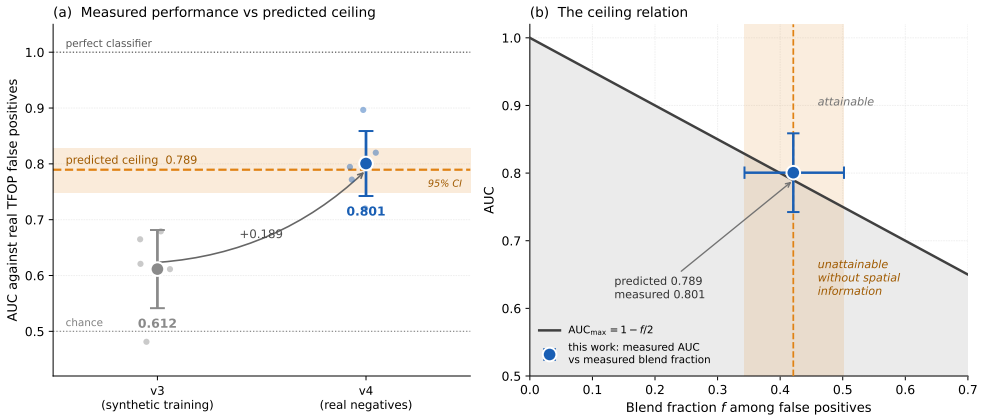


Fig. 4 The blend ceiling, determined independently twice. Panel (a): AUC against real TFOP false positives for the detector trained on synthetic negatives (v3) and after fine-tuning on real negatives (v4); small points are individual cross-validation folds, error bars the standard deviation across folds. The shaded band is the ceiling predicted from the measured blend fraction, $\mathrm{AUC}_{\max} = 1 - f/2$, with $f = 0.421$ [0.343, 0.502]. Panel (b): the ceiling relation as a function of blend fraction, with our measurement placed on it with uncertainties on both axes. The measured value lies 0.19σ from the independent prediction.

difference-image analysis of 145 false positives and nested cross-validation of the classifier — converge on the same value.

We conclude that the retrained detector operates at the ceiling imposed by the blend fraction, with no appreciable margin for improvement within the single-band photometric domain.

Two caveats bound this conclusion, and they operate in opposite directions. The assumption of perfect separability over the non-blends is optimistic, so that 0.789 constitutes an upper limit. Conversely, not all blends are wholly indistinguishable: a diluted eclipsing binary may retain a partially discriminating V-shaped profile, so that the effectively irresolvable fraction is somewhat smaller than 0.421. The observed agreement should therefore not be read as an exact equality, but as evidence that the remaining margin is small relative to the uncertainty of both determinations.

5 Application to unresolved TOIs

5.1 Application set

We applied the v4 detector to the set of TOIs with PC or APC disposition and period $P < 1.5$ d, excluded by construction from the training set for lacking ground truth. After requiring SPOC 120 s photometry and applying the preprocessing of Sect. 3.2, the set comprises 435 objects. These are candidates that have remained unresolved after TFOP follow-up, and therefore constitute the natural use case for a classifier intended to prioritise targets.

5.2 Scoring and centroid filtering

The score distribution is strongly bimodal: 140 objects exceed 0.5, 78 exceed 0.8 and 49 exceed 0.9, the threshold we adopt for subsequent analysis. The threshold is a free parameter of the pipeline, not a property of the detector: it fixes how many candidates enter the subsequent stages, and can be lowered or raised according to the vetting effort available (Sect. 6.3).

To those 49 we applied the difference-image analysis described in Sect. 3.4. Twenty-nine (59%) show the transit source displaced by more than one pixel from the target and are classified as blends, a proportion consistent with the fraction measured on the labelled false-positive set and with the expectation that the detector is blind to this class of contaminant. The remaining 20 retain a source coincident with the target.

We formalise the full procedure in **CASCADE-USP** (CNN-Assisted Sequential Centroid And Dilution Evaluation), a pipeline that chains photometric classification (Sect. 4) with difference-image centroid analysis (Sect. 3.4) and evaluation of dilution by contaminating sources through TRICERATOPS [27] and high-angular-resolution contrast curves, which it locates and retrieves automatically from ExoFOP. The design responds directly to the diagnosis of this work: since a substantial fraction of false positives is irresolvable from the light curve, the pipeline does not pursue a better classifier but the systematic incorporation of the information channels that photometry does not contain — source position through pixel-level analysis, and stellar field and unresolved companions through scenario modelling with high-resolution imaging [30]. Its output is not a verdict but a decision table which, for each candidate, additionally records *what information is missing for validation*, allowing observing time to be prioritised. The framework is independent of the period regime: only the classification stage is domain-specific, so that adaptation to other regimes reduces to retraining the classifier on the corresponding population.

5.3 Individual vetting

Table 4 lists the 20 surviving candidates with their scores, centroid offsets, Gaia RUWE values and outcome. Each was analysed individually through TRICERATOPS with contrast curves where available, complemented by inspection of the TFOP observing notes.

5.4 Score ordering

The validated object ranks 26th of 435 by score, and fifteenth among the 20 survivors. The two highest-scoring candidates (0.998 and 0.987) proved to be, respectively, an eclipsing binary on the target and a blend with NFPP = 1.

Comparing the 20 survivors with the 29 candidates rejected by the centroid test, the classifier score shows a weak but significant discriminating ability (AUC = 0.73, $p = 0.006$, Mann–Whitney): blends at separations above one pixel score somewhat lower, suggesting that their dilution leaves a residual detectable signature. The separation is nevertheless insufficient for operational use — the highest-scoring blend exceeds fifteen of the twenty survivors — and does not extend to the problem that matters: within the surviving set, the score *does not order by planetary likelihood*. This is the

Table 4 The 20 candidates surviving the centroid filter, ordered by v4 score. Offsets are difference-image centroid displacements (blend threshold 1.0 pixel). RUWE values are from Gaia DR3; entries above 1.4 are flagged as indicative of an unresolved companion [31]. Dashes denote sources without a published value.

TIC	TOI	P (d)	offset (px)	score	RUWE	Outcome
44797824	865.01	0.746	0.60	0.9979	1.12	EB on target (FPP 0.27)
465933345	6274.01	1.111	0.67	0.9868	1.06	blend (NFPP 1.00)
165412561	—	1.468	0.88	0.9842	**5.41**	chromatic blend
160522555	—	1.307	0.78	0.9751	0.91	V-shaped, NEBs uncleared
469782185	1123.01	1.209	0.60	0.9748	—	centroid offset (ExoFOP)
409315469	—	1.075	0.70	0.9729	1.05	chromatic blend
441600335	4159	0.866	0.55	0.9723	—	chromatic blend (FPP 0.26)
131195882	6597	0.910	0.45	0.9720	0.98	no ground-based detection
200001699	—	0.324	0.44	0.9717	**1.49**	blend (NFPP 0.38)
119290630	—	1.488	0.90	0.9697	1.01	no contrast curve
76835246	7483	0.513	0.35	0.9688	1.06	no high-resolution imaging
301455423	3326	1.066	0.75	0.9676	1.00	source on 3.9″ neighbour
366754985	—	1.447	0.49	0.9665	**2.52**	neighbours uncleared
288671122	—	0.287	0.65	0.9618	1.05	blend (NFPP 0.26)
418343229	**6662.01**	**0.294**	**0.94**	**0.9577**	**1.23**	**validated planet**
200606486	6209	0.748	0.99	0.9418	**4.25**	chromatic blend
90935995	6801.01	1.224	0.63	0.9384	0.99	low-contrast EB (FPP 0.07)
438777551	3161	1.401	0.89	0.9278	1.17	source on 98″ neighbour
441736986	5657.01	0.804	0.94	0.9087	0.90	blend: 2.2″ neighbour
124453339	3106.01	1.485	0.51	0.9005	**2.81**	unresolved companion

expected consequence of the result of Sect. 3.4: the upper end of the score distribution concentrates precisely the cleanest and deepest transit signals, which are also those producing the most convincing blends and binaries. The useful discrimination does not come from the detector's ranking but from the complementary information that the detector cannot see.

5.5 False-positive taxonomy

Of the twenty surviving candidates, nineteen fail the validation criteria. Classifying them by failure mode is more informative than their bare count, because *each class was resolved through a different information channel, and none of those channels is present in the folded light curve.*

(a) Chromatic blends — 4 objects

(TIC 165412561, 409315469, 441600335, 200606486). Multiband ground-based photometry reveals a marked dependence of transit depth on wavelength. TIC 165412561 goes from 5.67 ppt in g to 14.92 ppt in z; TIC 409315469 from 0.42 to 7.40 ppt between the same bands; TIC 441600335 shows a factor of forty between g and z_s. A planetary transit produces moderate chromatic variation through limb darkening, never of this

order. Such measurements were obtained with simultaneous multiband instruments such as MuSCAT2 [54]; the use of multicolour photometry to validate or reject ultra-short-period TESS candidates has direct precedent in Parviainen et al. [55]. *Channel required: colour.*

(b) Spatial blends — 7 objects

(TIC 465933345, 469782185, 200001699, 301455423, 288671122, 438777551, 441736986). The transit source is localised on a star other than the target, or the target is contaminated by a neighbour that cannot be separated. TIC 438777551 is the clearest case: ground-based photometry detects no transit on the target, while a neighbour at 98 arcsec shows a 25 ppt event. TIC 465933345 receives FPP = NFPP = 1.00 from TRICERATOPS.

TIC 441736986 deserves separate mention. Two independent ground-based detections report a ∼7–9 ppt event, but both apertures are contaminated by a neighbour at 2.2 arcsec with $\Delta T = 2.3$, bright enough to produce the observed event on its own, and neither observation can separate the pair: the seeing (5.2 arcsec FWHM) exceeds the separation by a factor of two. The TFOP notes state explicitly that a focused observation is still required to determine the source. Crucially, this object *passed* our centroid test with an offset of 0.94 pixels: at 2.2 arcsec the contaminant lies one tenth of a TESS pixel from the target, well within the regime identified in Sect. 3.4 as inaccessible to difference-image centroid analysis. It is a direct illustration of why the measured blend fraction is a lower bound. *Channel required: position, stellar field, and angular resolution below the TESS pixel scale.*

(c) Eclipsing binaries on target — 2 objects

(TIC 44797824, 90935995). The signal originates unambiguously on the target — TIC 44797824 obtains NFPP = 0.000, and follow-up with six MEarth telescopes [56] confirms the source — but statistical modelling favours eclipsing-binary scenarios over the planetary one. TIC 90935995, with a depth of 27 ppt, would imply a radius of approximately one Jupiter radius. In both cases the application of high-angular-resolution contrast curves reduces the FPP without reaching the validation threshold. *Channel required: scenario modelling plus high-resolution imaging.*

(d) Irreproducible signal or uncleared field — 3 objects

(TIC 131195882, 160522555, 366754985). Ground-based follow-up does not reproduce the event, or fails to clear the neighbouring stars in the field. *Channel required: independent photometry.*

(e) Insufficient data — 2 objects

(TIC 119290630, 76835246). These lack high-angular-resolution imaging, without which the FPP remains dominated by unresolved-companion scenarios. They are not demonstrated false positives but candidates that cannot be validated with the available information. *Channel required: high-resolution imaging.*

(f) Astrometric evidence of an unresolved companion — 1 object

We queried the Gaia DR3 renormalised unit weight error (RUWE) for all twenty surviving candidates. The parameter quantifies the goodness of fit of a single-star astrometric solution [31]: values near unity indicate a satisfactory solution, while elevated values indicate that the single-star model describes the data poorly, typically because of an unresolved companion. Thresholds adopted in the literature range from 1.25 [57] to 1.4 [31].

Eighteen candidates have a published value, of which *five (28%) exceed 1.4*, against the ∼12% characteristic of the *Kepler* sample: the surviving candidates are enriched in astrometric binarity by more than a factor of two. No candidate falls in the ambiguous interval between 1.25 and 1.4, so none of our conclusions depends on the choice of threshold.

Four of those five had already been rejected through independent channels — two by chromaticity, one by uncleared neighbours and one by elevated NFPP — so that astrometry independently confirms diagnoses reached by other routes. The concordance is physically expected in the chromatic cases: TIC 165412561 (RUWE = 5.41) and TIC 200606486 (RUWE = 4.25) are plausibly perturbed astrometrically by the same companion that produces the wavelength-dependent dilution — the same physical object detected through two independent channels.

The fifth, TIC 124453339, was flagged by astrometry alone. It presented the cleanest ground-based record of the sample: two independent detections of consistent depth (4.5 and 4.6 ppt) in uncontaminated apertures, with 21 of 23 neighbours cleared, no chromaticity and no centroid offset. It nevertheless carries RUWE = 2.81. Consistently, Gaia publishes no astrophysical parameters for this source and the TIC lacks both mass and parallax; TRICERATOPS reports insufficient information to validate it. Neither the photometry, nor the centroid analysis, nor the contrast curve flagged this object; the astrometric solution did.

The validated planet lies in the clean group (RUWE = 1.23), providing an additional independent line of support for its planetary nature.

We note that the channel is complementary rather than redundant: RUWE is sensitive to companions below the Gaia resolution limit, whereas resolved neighbours at several arcseconds — such as the contaminant 2.2″ from TIC 441736986, whose RUWE is 0.90 — require stellar-field modelling instead.

The central observation of this section is the following: *none of the nineteen false positives was distinguishable from a planetary transit on the basis of the folded TESS light curve.* All had passed automated filtering, the human vetting of the TESS Science Office, and our classifier with a score above 0.9; sixteen additionally passed the centroid test. Their nature was established through information on colour, position, the surrounding stellar field, independent photometry, or astrometry — channels all absent from the flux time series.

This carries a practical consequence beyond the specific case: *no single complementary test is sufficient.* TRICERATOPS resolves classes (b) and (c) but is blind to colour; multiband photometry resolves (a) but does not quantify binary scenarios; centroid analysis resolves blends at separations above one pixel but not closer ones; astrometry resolves unresolved companions but not resolved neighbours. Validating

an ultra-short-period candidate in TESS requires the concurrence of several independent channels, and the contribution of a photometric classifier is necessarily limited to prioritisation.

6 TOI-6662 b: an independent validation

6.1 Statistical validation

TOI-6662 b (TOI-6662.01, TIC 418343229) received a score of 0.958 from the v4 detector and passed the difference-image test with an offset of 0.94 pixels, consistent with an on-target origin. Its catalogued period is $P = 0.2939493$ d (7.05 h), and the host is an M dwarf of radius $R_\star = 0.332 \pm 0.010\,R_\odot$ and effective temperature $T_{\rm eff} = 3359 \pm 157$ K, observed by TESS in sectors 19, 20, 26 and 40.

We applied TRICERATOPS [27] to the folded and binned light curve, with the stellar field drawn from TRILEGAL and fifteen independent realisations of 5×10^5 samples each. Without high-resolution imaging information, the false-positive probability is FPP = 0.061, placing the object in the *likely planet* category but short of the validation threshold. Incorporating the contrast curve obtained with the Gemini speckle interferometer in the 832 nm band [30], the values drop to FPP = 0.0035 and NFPP = 0.00050 across all fifteen realisations (Fig. 5). Both satisfy the validation criteria of Giacalone et al. [27], which require FPP < 0.015 and NFPP $< 10^{-3}$. **TOI-6662 b is therefore statistically validated as a planet.**

The factor of seventeen reduction in FPP on incorporating the contrast curve illustrates the point developed in Sect. 5.5: high-angular-resolution imaging information, absent from the photometry, is what resolves the unresolved-companion scenarios that dominated the residual probability.

A further channel supports the validation: TOI-6662 b has RUWE = 1.23 in Gaia DR3, below the thresholds conventionally adopted as indicative of an anomalous astrometric solution [31, 57], with no evidence therefore of an unresolved companion.

The target benefits from unusually extensive high-resolution imaging coverage: ExoFOP records six speckle observations from four instruments — Gemini/'Alopeke at 562 and 832 nm, WIYN/NESSI at the same two bands, and two epochs with the SAI-2.5m Speckle Polarimeter in I — with contrast limits between Δ4.5 and Δ6.8 mag. The validation adopts the deepest of these, but the concordance of four independent instruments strengthens the exclusion of resolved companions.

6.2 Consistency with TFOP follow-up

The statistical validation agrees with independent follow-up. The object has five ground-based photometric detections of the event, all in uncontaminated apertures and consistent in time and duration with the ephemeris. The TFOP notes state that no further observations are required beyond extreme-precision photometry aimed at characterising transit-timing variations, which reflects that the follow-up programme already treats the object as planetary. The apparent chromatic dependence of the depth is accounted for by the faintness of the M-dwarf host in the blue.

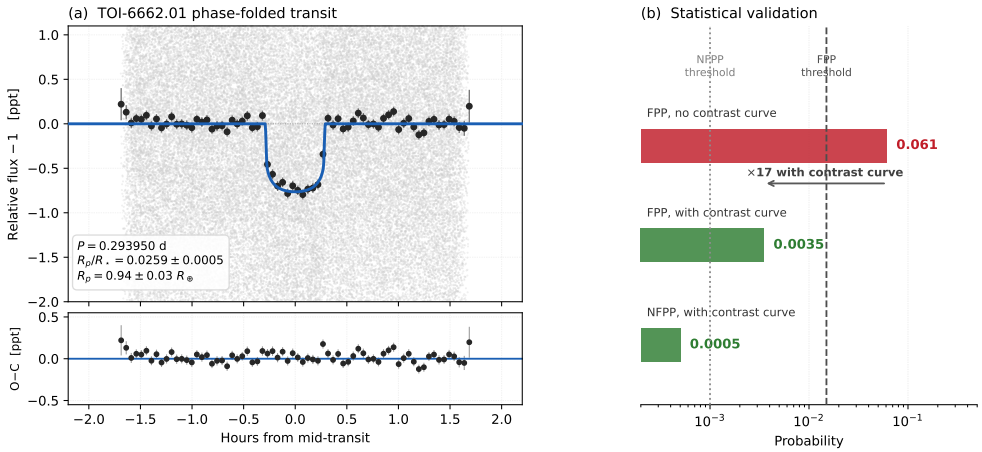


Fig. 5 TOI-6662 b. Panel (a): phase-folded photometry from sectors 19, 20, 26 and 40 (grey), binned means with standard errors (black), and the best-fit `juliet` transit model (blue); residuals below. Panel (b): false-positive probabilities from TRICERATOPS with and without the Gemini 832 nm speckle contrast curve, against the validation thresholds of Giacalone et al. [27]. Incorporating the contrast curve lowers the FPP by a factor of 17 and moves the candidate across the validation threshold.

6.3 Comparison with an independent validation

After the submission of this work, Collier et al. [28] published a statistical validation of the same object, designated TOI-6662 b, within an automated TRICERATOPS analysis of 443 TESS candidates designed to measure the contribution of high-resolution imaging to validation. The two analyses were carried out independently and reached the object by different routes. In Collier et al. [28] it entered through a target list drawn from TFOP planet candidates in predefined categories of parameter space; here it was recovered from a pool of 435 unresolved TOIs by classifier prioritisation followed by spatial vetting, which is precisely the task CASCADE was designed for. Table 5 compares the quantities the two works have in common.

The transit geometry agrees within one standard deviation in radius ratio, scaled semi-major axis and planetary radius. The classification agrees as well, and so does the role of the imaging: both analyses find the object short of the validation threshold without the contrast curve ($\mathrm{FPP}_{\mathrm{noCC}} = 0.061$ here, 0.026 there) and well inside it with the curve. The absolute FPP values with the curve differ by several orders of magnitude, which is expected at this level: once the competing scenarios are suppressed, the residual FPP depends sensitively on light curve preparation, ephemeris and sampling, and what is robust is the classification, not the figure. Our fitted period, $P = 0.293950$ d (Fig. 5), coincides with theirs to the precision quoted; the catalogued value used to set up the analysis, $P = 0.2939493$ d, differs from it by 8×10^{-7} d, which accumulates to about two minutes over the baseline from sector 19 to sector 40, small against a transit duration of ∼35 minutes.

The agreement must not be overstated. Both analyses rest on SPOC photometry, on TRICERATOPS with its priors, and on a Gemini/'Alopeke contrast curve

Table 5 TOI-6662 b in this work and in Collier et al. [28]. FPP values are means over independent TRICERATOPS realisations (15 of 5×10^5 samples here; 20 of 10^6 there). $\mathrm{FPP_{noCC}}$ is the value obtained without the contrast curve. Masses are estimated from the mass–radius relation of Chen and Kipping [58] in both works.

Quantity	This work	Collier et al. [28]
P (d)	0.293950	$0.29395013^{+0.00000005}_{-0.00000006}$
$R_p/R_\star$	0.0259 ± 0.0005	$0.0260^{+0.0005}_{-0.0006}$
$a/R_\star$	3.81 ± 0.14	$3.85^{+0.12}_{-0.14}$
R_p ($R_\oplus$)	0.94 ± 0.03	$0.94^{+0.03}_{-0.04}$
M_p ($M_\oplus$, estimated)	≈ 0.8	0.78
FPP (with contrast curve)	3.5×10^{-3}	1.6×10^{-11}
$\mathrm{FPP_{noCC}}$	0.061	0.026
NFPP	5.0×10^{-4}	$< 10^{-3}$
Contrast curve	'Alopeke, 832 nm	'Alopeke, 832 nm
Gaia DR3 RUWE	1.23	≤ 1.4 (cut)
Centroid test	0.94 px offset	—

at 832 nm; they share their principal inputs. What the comparison establishes is that the validation is reproducible under two independent implementations, not that it rests on two independent bodies of evidence. The elements of our analysis without a counterpart in theirs — the difference-image centroid test, the review of six speckle observations from four instruments, and the five ground-based detections in uncontaminated apertures — add to the case, while both apply the Gaia astrometric cut.

For CASCADE the comparison has a specific value. A candidate prioritised by the classifier, filtered by its centroid and resolved by scene modelling reaches the same verdict as a dedicated validation effort with access to the same follow-up. It is the closest available approximation to an end-to-end external test of the pipeline on a positive case, and it is the natural end point of the procedure described in this work.

The comparison also permits a test in the opposite direction. Collier et al. [28] validate two further ultra-short-period planets within our period range, TOI-1435 b ($P = 0.686$ d) and TOI-1806 c ($P = 0.502$ d). Both belong to our application set of 435 TOIs, and neither reached the centroid stage: the v4 detector assigned them scores of 0.29 and 0.10, ranking them 200th and 274th. Of the three planets in the application set validated by Collier et al. [28], CASCADE therefore recovers one at its operating threshold of 0.9. These are false negatives of the classifier, not of the spatial filters, so they leave the blend fraction of Sect. 3.4 unaffected; but they measure, on real planets, the cost of a threshold chosen for purity, and they agree with the conclusion of Sect. 5.4 that the score orders candidates for follow-up rather than by planetary likelihood. Both signals are less favourable for single-band detection than that of TOI-6662 b: TOI-1435 b has a transit depth of ∼150 ppm against ∼680 ppm, and TOI-1806 c orbits a host nearly two magnitudes fainter ($T = 12.6$ against 10.9; Collier et al. 28).

Both would have been recoverable at a lower threshold, at a price that can be stated exactly. Lowering it to 0.29 would have admitted TOI-1435 b, with 201 candidates entering the centroid stage instead of 49; admitting TOI-1806 c as well would have required 0.10, and 274 candidates, 63% of the set. Since the classifier costs nothing to run, while the stages after it — the centroid analysis and, above all, the individual vetting of the survivors — are where the effort lies, the threshold should be set by the follow-up budget available rather than fixed in advance: a survey seeking purity with limited resources operates high, one seeking completeness operates low and accepts a proportionally larger vetting load. With only three validated planets in the application set, we do not attempt to calibrate a completeness curve as a function of the threshold; the figures above illustrate the trade-off rather than measure it.

6.4 Transit fit

We fitted the transit with `juliet` [59], which models the transit through `batman` [60] and explores the parameter space by nested sampling with `dynesty` [61]. To keep the problem tractable given the ∼350 transits present in four sectors, we extracted windows of ±3 transit durations centred on each predicted event and normalised each window by its local out-of-transit median.

We fitted period, epoch, radius ratio, impact parameter and stellar density — the last with a Gaussian prior derived from the TIC parameters, which breaks the degeneracy between impact parameter and radius ratio — with quadratic limb darkening in the parametrisation of Kipping [62] and a white-noise jitter term. The eccentricity was fixed to zero, a choice justified in Sect. 6.5.

We obtain $R_p/R_\star = 0.0259 \pm 0.0005$ and $b = 0.28^{+0.12}_{-0.17}$. Combined with $R_\star = 0.332 \pm 0.010\,R_\odot$, this yields $R_p = 0.94 \pm 0.03\,R_\oplus$, with the uncertainty dominated by that of the stellar radius. TOI-6662 b is therefore an Earth-sized planet.

6.5 Tidal environment

With a semi-major axis of $a/R_\star = 3.81 \pm 0.14$, TOI-6662 b orbits at 1.19 ± 0.01 times the tidal disruption distance (fluid Roche limit). This proximity imposes a minimum bulk density on the planet — close to the terrestrial value — below which it would have been disrupted at this separation, the minimum-density argument established by Rappaport et al. [6] for the 4.2 h planet KOI-1843.03.

Adopting $M_p \approx 0.8\,M_\oplus$ estimated from the mass–radius relation of Chen and Kipping [58], the orbital decay timescale due to stellar tidal dissipation, in the constant-lag model [63], is approximately $20\,(Q'_\star/10^7)$ Gyr. For the limit $Q'_\star \gtrsim 10^7$ inferred at the population level for ultra-short-period planets by Hamer and Schlaufman [64], the orbit is stable against tidal inspiral on timescales comparable to the age of the system. At this period tidal circularisation is essentially instantaneous in astronomical terms, which supports the assumption of a circular orbit adopted in the fit.

6.6 Physical characterisation

The planet receives 366^{+79}_{-67} times the terrestrial irradiation. Its equilibrium temperature, assuming zero albedo and full heat redistribution ($f = 1/4$), is ∼1220 K, rising

to ∼1555 K on the dayside in the absence of redistribution [$f = 2/3$; 65]. These values place TOI-6662 b at the boundary of the regime where a surface magma ocean can be sustained: comparable dayside temperatures have been considered insufficient for that purpose [9, 66]. It is therefore not unambiguously a lava world, but a body for which the state of the mantle depends on factors beyond the irradiation alone — in particular on any residual tidal heating — which makes it an object of interest for future phase-curve measurements. Collier et al. [28] report an emission spectroscopy metric of 12.0, the highest among the terrestrial planets they newly validate, above the threshold of 7.5 recommended by Kempton et al. [67] for JWST follow-up.

With $R_p = 0.94\,R_\oplus$ and an irradiation far above 100 $S_\oplus$, the planet lies unambiguously in the lower rocky peak of the radius valley [5], consistent with a core stripped of its envelope by photoevaporation — the "hot super-Earth desert" described by Lundkvist et al. [4].

6.7 Context

At $P = 0.294$ d, TOI-6662 b falls comfortably within the ultra-short-period regime, defined by $P < 1$ d [3]. It is not a record: the shortest-period confirmed planet is K2-137 b, at 0.18 d around a $0.463\,M_\odot$ M dwarf [68], and the candidate KOI-1843.03 has a still shorter period [6]. Among Earth-sized planets with $P < 0.42$ d it ranks seventh of eighteen by period and is the smallest of the four M-dwarf hosts with comparable periods (Figs. 6 and 7).

Its closest analogues are TOI-6255 b (0.238 d, $1.08\,R_\oplus$; Dai et al. 69), TOI-6324 b (0.279 d, $1.06\,R_\oplus$; Lee et al. 70) and TOI-4552 b (0.301 d, $1.11 \pm 0.04\,R_\oplus$, $\rho_p = 7.74 \pm 2.12$ g cm^{-3}, M4.5V host at 27.26 pc; Srivastava et al. 9), all Earth-sized planets around M dwarfs with periods within 20% of ours; its radius places it alongside the dense sub-Earths such as GJ 367 b [7], and its proximity to the Roche limit relates it to TOI-6255 b, described as a planet on the verge of tidal disruption. In all these cases, however, the planetary nature was established through radial velocities or high-angular-resolution imaging with a mass determination. Only around a dozen ultra-short-period rocky planets orbiting M dwarfs have both mass and radius determined [9]; TOI-6662 b is not among them.

Its interest lies not, therefore, in a superior characterisation relative to its peers, but in the route by which it was identified: the recovery of an unresolved candidate from the TOI catalogue through automated prioritisation. In a regime where the occurrence rate of terrestrial USPs around M dwarfs peaks [8] but the distinction from false positives is hardest, this is precisely the kind of object that an honestly characterised classifier can help to rescue — provided its output is read as what it is: a prioritisation, not a decision.

We emphasise that this is a statistical validation, not a dynamical confirmation. The mass remains unmeasured, and definitive confirmation would require radial velocities or the analysis of transit-timing variations currently pursued by TFOP. The expected radial-velocity semi-amplitude, ≈ 1.6 m s^{-1} for the inferred mass, is accessible to high-stability near-infrared spectrographs given the brightness of the host ($T = 10.9$).

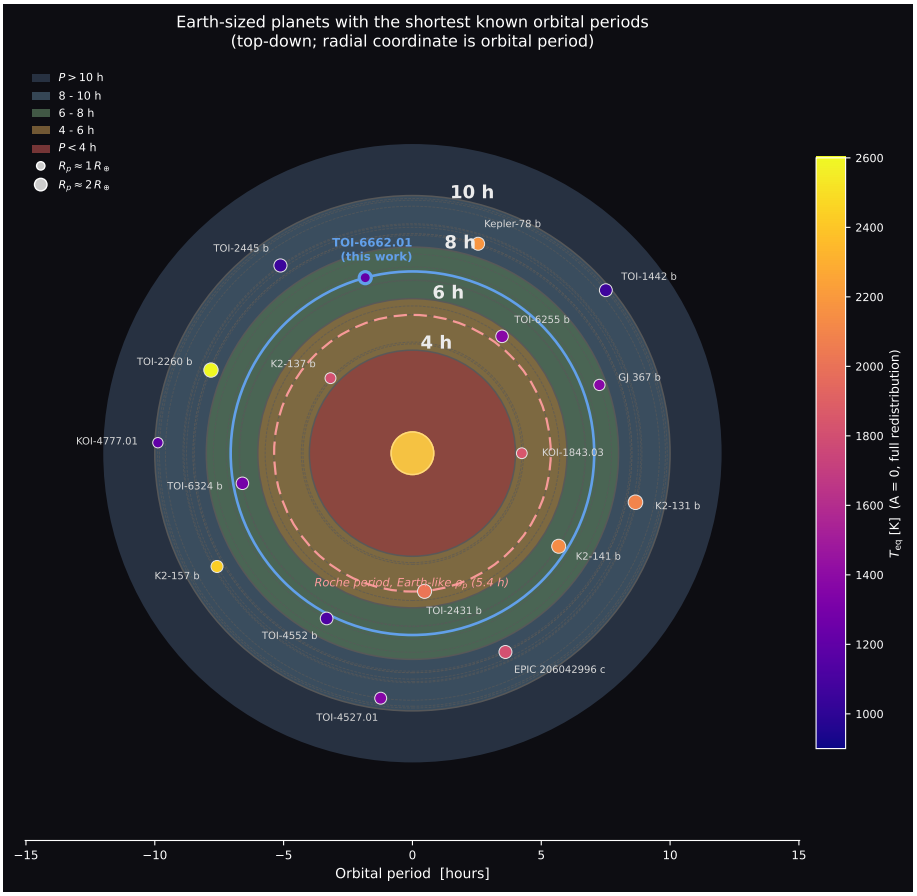


Fig. 6 Earth-sized planets with the shortest known orbital periods, viewed top-down with the radial coordinate set by orbital period. Coloured bands mark period intervals; the dashed ring indicates the Roche-limiting period for an Earth-like bulk density (5.4 h; Rappaport et al. 6). Symbol colour encodes equilibrium temperature (zero albedo, full redistribution) and symbol size scales with planetary radius. TOI-6662 b, validated independently in this work and by Collier et al. [28], is highlighted.

7 Discussion

7.1 The blend ceiling as a fundamental limit

The central result of this work is not the performance of a particular detector, but the existence of a structural limit from which no single-band photometric detector can escape. Two methodologically independent determinations place it at the same value. On the one hand, difference-image analysis establishes that 42% of real false positives are blends (Sect. 3.4); under the assumption that these are indistinguishable from transits in the light curve, the maximum attainable AUC is $1 - f/2 = 0.789$. On the other, retraining with real negatives, evaluated under nested cross-validation, reaches 0.80 ± 0.06 (Sect. 4.4). That a prediction derived from the blend fraction and a measurement of the classifier should agree to the second decimal place is no

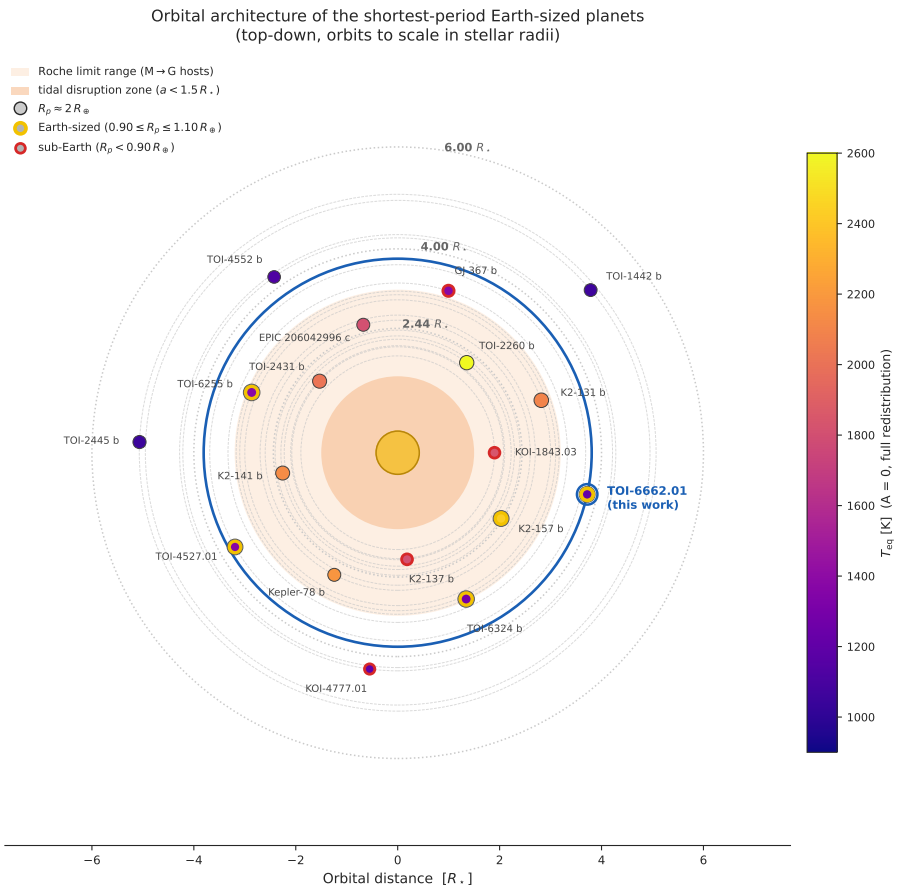


Fig. 7 Orbital architecture of the same sample, with orbits to scale in units of stellar radius. Shaded regions indicate the range spanned by the Roche limit across host spectral types and the inner tidal disruption zone. Earth-sized planets ($0.90 \le R_p \le 1.10\,R_\oplus$) are outlined in yellow and sub-Earths ($R_p < 0.90\,R_\oplus$) in red.

coincidence: it is the signature of a detector that has learned everything learnable, with the remainder not residing in the data it consumes.

The consequence is uncomfortable for the dominant line of research. *Progress in photometric transit detection with neural networks is limited neither by architecture, nor by training-set size, nor by computing power, but by the physical information contained in a single-band light curve.* No innovation along those three axes — deeper networks, more synthetic data, more GPUs — can surpass the ceiling, because the ceiling lies not in the model but in the absence of the discriminating signal at its input. The irreducible fraction we measure is moreover a lower bound: at the resolution of one TESS pixel, blends from closer neighbours escape our test and would raise the barrier further.

The way out is not photometric. It lies in incorporating the information channels that do distinguish a blend from a planet: colour, through multiband photometry;

position, through centroid analysis or high-resolution imaging; the stellar field, through scene modelling; and, as this work adds, astrometry, through the quality of the single-star solution.

This conclusion is not speculative: it reflects the direction the field has itself taken. ExoMiner [16] incorporates centroid motion data among its inputs; Tardugno Poleo et al. [20] add background flux and centroid information to a convolutional classifier, identifying a median 18% of contaminants; and the TRICERATOPS+ extension [71] adds ground-based multiband photometry to the validation framework, integrating precisely the colour channel whose absence from the light curve we identify as responsible for the irreducible fraction of chromatic blends. Breaking the photometric ceiling proceeds, in current practice, through the incorporation of exactly the channels this work identifies.

7.2 Implications for detector benchmarking

Our results compel a reconsideration of the established practice of evaluating transit detectors against synthetic or catalogued eclipsing binaries. The same detector that attains an AUC of 0.97 against the binaries of Prša et al. [35] obtains 0.50 — pure chance — against the real false positives of TFOP with an identical positive class (Sect. 3.3). The difference is neither marginal nor attributable to the composition of the positive sample, which we held fixed: it is the difference between an apparently solved classifier and one with no discriminating power at all.

This carries a direct implication, which we state without circumlocution: *the near-unity AUC values that punctuate the deep-learning transit literature — 0.988, 0.999, 1.0 — do not measure the ability of these systems to operate on real data, but their ability to solve a problem easier than the real one.* We do not question the technical correctness of those works; we question that the reported metric is informative about production performance. A detector evaluated exclusively against eclipsing binaries has not been evaluated on the population that will determine its false-positive rate in a real search.

We therefore propose that the evaluation of any transit detector intended for TESS data include, as a requirement rather than a complement, a test set built from real TFOP false positives — objects that passed automated filtering and human vetting before being rejected by follow-up. It is the only set that represents the true difficulty of the task. Reporting an AUC against synthetic binaries without accompanying it with this second figure should be regarded as an incomplete characterisation of performance.

The subtlety of the problem is illustrated within our own work. In retraining the detector, a cross-validation protocol selecting the stopping epoch by performance on the test fold — an apparently innocuous practice — inflated the AUC by 0.040 (Sect. 4.3), a magnitude comparable to those customarily invoked to establish the superiority of one architecture over another. Evaluation bias is not a defect of others: it is a standing temptation that only a strict protocol — nested cross-validation, representative test sets — keeps at bay.

We add a practical recommendation. The Gaia RUWE query is the cheapest of the channels employed here: a single call to a catalogue service, of order one second

per target, against minutes for scenario modelling and days to months for ground-based follow-up. Applied on its own to our sample it would have flagged five of the nineteen false positives (26%) with no observational effort whatsoever. We recommend its inclusion as an early filter in any candidate-vetting pipeline.

7.3 Limitations

We enumerate the limitations of this work, some of which bound the scope of the preceding conclusions.

The blend fraction of 42% is a lower bound, not a complete measurement: our centroid test, with a threshold of one pixel (21 arcsec), is blind to blends produced by neighbours at smaller separations, which TRICERATOPS does capture through the NFPP but which escape population-level characterisation. TIC 441736986 illustrates the point directly: its contaminant lies 2.2 arcsec away, one tenth of a TESS pixel, and the object passed our test with an offset of 0.94 pixels. The true ceiling of the photometric domain is therefore probably above 0.789.

The retraining set is small (364 curves), which lends the AUC figure an appreciable uncertainty (± 0.06) and makes the procedure sensitive to the evaluation protocol. The positive class further inherits the selection bias of the confirmed catalogue towards bright objects with deep transits.

The detector does not reach the shortest-period regime. The transit search algorithm used in the survey phase presents an effective floor around $P \approx 0.6$ d on two-minute photometry, so that planets of shorter period — including the most extreme, such as analogues of KOI-1843.03 — lie beyond its reach. The validation of TOI-6662 b ($P = 0.294$ d) was possible because the object already appeared in the TOI catalogue, not because our survey could have recovered it.

Finally, the validation of TOI-6662 b is statistical: its mass has not been measured, and its planetary nature, although established with high confidence through the concurrence of FPP, centroid analysis, contrast curve, astrometry and ground-based follow-up, does not amount to a dynamical confirmation. Nor is the pipeline complete at its operating threshold: two planets of the application set validated by Collier et al. [28] scored below 0.9 and were not recovered (Sect. 6.3). We did not conduct a systematic search for additional planets in the system; the detection of companions on wider orbits is left for future work.

7.4 TOI-6662 b in context

The validation procedure employed here — photometric classification, centroid analysis, TRICERATOPS with a speckle contrast curve, and confirmation through multiband ground-based photometry — reproduces that recently applied to TOI-4552 b [9]. In that case, however, as in those of its other analogues, the characterisation was completed with a mass determination from radial velocities.

Its interest lies not, therefore, in a superior characterisation, but in the route by which it was identified: the recovery of an unresolved candidate from the TOI catalogue through automated prioritisation. In a regime where the occurrence rate of terrestrial USPs around M dwarfs peaks [8] but the distinction from false positives is

hardest, this is precisely the kind of object that an honestly characterised classifier can help to rescue. That the object was reached independently by a dedicated validation programme [28] does not diminish this point; it confirms that the route through CASCADE leads to the right answer.

The framework of CASCADE is independent of the period regime: the centroid analysis and dilution evaluation stages operate on any transit candidate. Only the classification stage is domain-specific, so that adaptation to other regimes reduces to retraining the classifier on the corresponding population.

8 Conclusions

We have presented the construction, honest characterisation and application of a convolutional transit detector for ultra-short-period planets in TESS. Our conclusions are as follows.

1. The performance of a transit classifier evaluated against catalogued eclipsing binaries does not predict its operational performance. Our detector attains an AUC of 0.97 against the binaries of Prša et al. [35] and **0.50 — indistinguishable from chance — against the real false positives of TFOP**, with an identical positive class. A factorial design varying each class separately attributes the degradation almost entirely to the nature of the negatives (Sect. 3.3).
2. The origin of the limit is physical, not algorithmic. Difference-image analysis of 145 real false positives establishes that **42.1% (95% CI: 34.3–50.2%) are blends**: genuine eclipses originating in a source other than the target, whose discrimination requires spatial information absent from the light curve. This fraction is a lower bound, since the one-pixel threshold (21 arcsec) does not resolve closer neighbours (Sect. 3.4).
3. Retraining with real false positives raises the AUC from 0.61 to 0.8006 ± 0.0582 under nested cross-validation. This value converges on the ceiling predicted independently from the blend fraction, $\mathrm{AUC}_{\max} = 1 - f/2 = \mathbf{0.789}$: two methodologically distinct determinations agree, indicating that the detector operates at the limit attainable within the single-band photometric domain (Sect. 4.4).
4. We document two manifestations of the same phenomenon within our own work. An earlier version of the detector learned a geometric shortcut — the V shape of the primary transit — introduced inadvertently by the negative generator, in the sense described by Geirhos et al. [22], attaining a synthetic AUC of 0.99 while its real performance collapsed (Sect. 2.3). And a non-nested cross-validation protocol inflated the AUC by **0.040**, a magnitude comparable to those customarily invoked to establish superiority between architectures (Sect. 4.3).
5. Applied to 435 unresolved TOIs, the **CASCADE-USP** pipeline yields 49 candidates scoring above 0.9, of which 29 are identified as blends. Of the remaining 20, **one proves to be a validated planet and 19 false positives**, documented individually by cause: chromatic blends, spatial blends, eclipsing binaries on target, irreproducible signals, astrometric binaries, and candidates lacking sufficient data. **None of the 19 was distinguishable from a planet on the TESS light curve alone** (Sect. 5).

6. The validated object ranks 26th of 435 by classifier score, while the two highest-scoring candidates proved to be an eclipsing binary and a blend with NFPP = 1. **The detector score does not rank by planetary likelihood** among the survivors; its contribution is limited to prioritisation (Sect. 5.4).
7. We introduce the Gaia RUWE as an additional vetting channel, independent of photometry, centroid and contrast curve. Of the eighteen surviving candidates with a published value, five (28%) exceed the threshold of 1.4, against the ∼12% characteristic of the *Kepler* sample. Four of the five had already been rejected through other channels — astrometry confirming them independently — and one was flagged by astrometry alone, despite presenting the cleanest ground-based record of the sample (Sect. 5.5).
8. We statistically validate **TOI-6662 b** (TOI-6662.01, TIC 418343229) with FPP = 0.0035 and NFPP = 0.00050, satisfying the criteria of Giacalone et al. [27], independently of the concurrent validation by Collier et al. [28], with which it agrees in radius ratio, scaled semi-major axis, planetary radius, classification and dependence on the contrast curve. This agreement closes the CASCADE procedure with an external check on a real planet. The transit fit yields $\mathbf{R_p = 0.94 \pm 0.03\,R_\oplus}$ with $P = 0.2939$ d around an M dwarf of $0.332\,R_\odot$. The planet receives 366 times the terrestrial irradiation, reaching an equilibrium temperature of ∼1220 K, orbits at 1.19 times its tidal disruption limit — which imposes a minimum density consistent with a rocky composition — and has an orbital decay timescale of ∼20 $(Q'_\star/10^7)$ Gyr, stable against tidal inspiral (Sect. 6).
9. We recommend that the evaluation of any transit detector intended for TESS data include, as a requirement rather than a complement, a test set built from real TFOP false positives. An AUC obtained exclusively against synthetic or catalogued eclipsing binaries constitutes an incomplete characterisation of operational performance (Sect. 7.2).
10. Breaking the photometric ceiling proceeds not through deeper architectures or larger training sets, but through the incorporation of the information channels absent from single-band photometry — colour, position, stellar field and astrometry — a direction confirmed by recent practice with the inclusion of centroid data in ExoMiner [16] and multiband photometry in TRICERATOPS+ [71] (Sect. 7.1).

Future work.

Dynamical confirmation of TOI-6662 b requires a mass measurement; the expected radial-velocity semi-amplitude, ≈ 1.6 m s^{-1} for the mass inferred from the mass–radius relation, is accessible to high-stability near-infrared spectrographs given the brightness of the host ($T = 10.9$). The framework of CASCADE is independent of the period regime: the centroid and dilution evaluation stages operate on any transit candidate, so that adaptation to other regimes reduces to retraining the classifier on the corresponding population.

Declarations

Funding. This research received no specific grant from any funding agency in the public, commercial or not-for-profit sectors.

Competing interests. The author declares no competing interests.

Ethics approval. Not applicable.

Data availability. The CASCADE code, the datasets used, and the intermediate results supporting the figures and tables in this article are provided as supplementary material accompanying this submission. Upon acceptance, they will be deposited in a permanent public repository and the persistent identifier will be inserted in the camera-ready version.

Software. `lightkurve` [45], `TRICERATOPS` [27], `juliet` [59], `batman` [60], `dynesty` [61], `transitleastsquares`, `astroquery`, `astropy`, `numpy`, `scipy`, `scikit-learn`, `matplotlib`, `PyTorch`.

Acknowledgements. This paper includes data collected by the TESS mission, obtained from the Mikulski Archive for Space Telescopes (MAST). Funding for the TESS mission is provided by NASA's Science Mission Directorate. This research has made use of the Exoplanet Follow-up Observation Program (ExoFOP; DOI: 10.26134/ExoFOP5) website, which is operated by the California Institute of Technology, under contract with the National Aeronautics and Space Administration under the Exoplanet Exploration Program. This work has made use of data from the European Space Agency (ESA) mission *Gaia* (https://www.cosmos.esa.int/gaia), processed by the Gaia Data Processing and Analysis Consortium (DPAC). We acknowledge the use of TESS Follow-up Observing Program (TFOP) data in this work.

References

[1] Léger, A., Rouan, D., Schneider, J., *et al.*: Transiting exoplanets from the CoRoT space mission. VIII. CoRoT-7b: the first super-earth with measured radius. Astron. Astrophys. **506**(1), 287–302 (2009) 0908.0241

[2] Batalha, N.M., Borucki, W.J., Bryson, S.T., *et al.*: Kepler's first rocky planet: Kepler-10b. Astrophys. J. **729**(1), 27 (2011) https://doi.org/10.1088/0004-637X/729/1/27

[3] Winn, J.N., Sanchis-Ojeda, R., Rappaport, S.: Kepler-78 and the ultra-short-period planets. New Astronomy Reviews **83**, 37–48 (2018)

[4] Lundkvist, M.S., Kjeldsen, H., Albrecht, S., *et al.*: Hot super-earths stripped by their host stars. Nature Communications **7**, 11201 (2016) https://doi.org/10.1038/ncomms11201

[5] Fulton, B.J., Petigura, E.A., Howard, A.W., *et al.*: The California-Kepler survey. III. a gap in the radius distribution of small planets. Astron. J. **154**(3), 109 (2017) https://doi.org/10.3847/1538-3881/aa80eb

[6] Rappaport, S., Sanchis-Ojeda, R., Rogers, L.A., Levine, A., Winn, J.N.: The Roche limit for close-orbiting planets: Minimum density, composition constraints, and application to the 4.2 hr planet KOI 1843.03. Astrophys. J. Lett. **773**(1), 15 (2013) https://doi.org/10.1088/2041-8205/773/1/L15

[7] Lam, K.W.F., Csizmadia, S., Astudillo-Defru, N., *et al.*: GJ 367b: A dense, ultrashort-period sub-earth planet transiting a nearby red dwarf star. Science **374**(6572), 1271–1275 (2021) https://doi.org/10.1126/science.aay3253

[8] Sanchis-Ojeda, R., Rappaport, S., Winn, J.N., *et al.*: A study of the shortest-period planets found with Kepler. Astrophys. J. **787**(1), 47 (2014) https://doi.org/10.1088/0004-637X/787/1/47

[9] Srivastava, A., Doyon, R., Bouchy, F., *et al.*: TOI-4552 b: A new ultra-short-period rocky world revealed by NIRPS and TESS. Astron. Astrophys. **709**, 73 (2026)

[10] Shallue, C.J., Vanderburg, A.: Identifying exoplanets with deep learning: A five-planet resonant chain around Kepler-80 and an eighth planet around Kepler-90. Astron. J. **155**(2), 94 (2018) https://doi.org/10.3847/1538-3881/aa9e09

[11] Ansdell, M., Ioannou, Y., Osborn, H.P., *et al.*: Scientific domain knowledge improves exoplanet transit classification with deep learning. Astrophys. J. Lett. **869**(1), 7 (2018)

[12] Yu, L., Vanderburg, A., Huang, C., *et al.*: Identifying exoplanets with deep learning. III. automated triage and vetting of TESS candidates. Astron. J. **158**(1), 25 (2019) https://doi.org/10.3847/1538-3881/ab21d6

[13] Osborn, H.P., Ansdell, M., Ioannou, Y., *et al.*: Rapid classification of TESS planet candidates with convolutional neural networks. Astron. Astrophys. **633**, 53 (2020)

[14] Tey, E., Moldovan, D., Kunimoto, M., *et al.*: Identifying exoplanets with deep learning. V. improved light-curve classification for TESS full-frame image observations. Astron. J. **165**(3), 95 (2023)

[15] Armstrong, D.J., Gamper, J., Damoulas, T.: Exoplanet validation with machine learning: 50 new validated Kepler planets. Mon. Not. R. Astron. Soc. **504**(4), 5327–5344 (2021) https://doi.org/10.1093/mnras/staa2498

[16] Valizadegan, H., Martinho, M.J.S., Wilkens, L.S., *et al.*: ExoMiner: A highly accurate and explainable deep learning classifier that validates 301 new exoplanets.

Astrophys. J. **926**(2), 120 (2022) https://doi.org/10.3847/1538-4357/ac4399

[17] Valizadegan, H., Martinho, M.J.S., Jenkins, J.M., *et al.*: Multiplicity boost of transit signal classifiers: Validation of 69 new exoplanets using the multiplicity boost of ExoMiner. Astron. J. (2023) https://doi.org/10.3847/1538-3881/acd344

[18] Wang, K., Ge, J., Willis, K., Wang, K., Zhao, Y., Hu, Q.: Discovery of small ultra-short-period planets orbiting Kepler KG dwarfs with GPU phase folding and deep learning. Mon. Not. R. Astron. Soc. **534**(3), 1913–1927 (2024) https://doi.org/10.1093/mnras/stae2155

[19] Salinas, H., Brahm, R., Olmschenk, G., Barry, R.K., Ishitani Silva, S., Araujo, V.: Exoplanet transit candidate identification in TESS full-frame images via a transformer-based algorithm. Mon. Not. R. Astron. Soc. **538**(3), 2031–2049 (2025) https://doi.org/10.1093/mnras/staf347

[20] Tardugno Poleo, V., Eisner, N.L., Hogg, D.W.: NotPlaNET: Removing false positives from planet hunters TESS with machine learning. Astron. J. **168**(3), 100 (2024) https://doi.org/10.3847/1538-3881/ad5f29

[21] Huertas-Company, M., Lanusse, F.: The dawes review 10: The impact of deep learning for the analysis of galaxy surveys. Publ. Astron. Soc. Aust. **40**, 001 (2023) 2210.01813

[22] Geirhos, R., Jacobsen, J.-H., Michaelis, C., Zemel, R., Brendel, W., Bethge, M., Wichmann, F.A.: Shortcut learning in deep neural networks. Nature Machine Intelligence **2**(11), 665–673 (2020) https://doi.org/10.1038/s42256-020-00257-z

[23] Lapuschkin, S., Wäldchen, S., Binder, A., Montavon, G., Samek, W., Müller, K.-R.: Unmasking clever hans predictors and assessing what machines really learn. Nature Communications **10**(1), 1096 (2019) https://doi.org/10.1038/s41467-019-08987-4

[24] Dhar, S., Shamir, L.: Systematic biases when using deep neural networks for annotating large catalogs of astronomical images. Astronomy and Computing **38**, 100545 (2022) https://doi.org/10.1016/j.ascom.2022.100545

[25] Ricker, G.R., Winn, J.N., Vanderspek, R., *et al.*: Transiting exoplanet survey satellite. Journal of Astronomical Telescopes, Instruments, and Systems **1**(1), 014003 (2015) https://doi.org/10.1117/1.JATIS.1.1.014003

[26] Twicken, J.D., Catanzarite, J.H., Clarke, B.D., *et al.*: Kepler data validation I—architecture, diagnostic tests, and data products for vetting transiting planet candidates. Publ. Astron. Soc. Pac. **130**(988), 064502 (2018) https://doi.org/10.1088/1538-3873/aab694

[27] Giacalone, S., Dressing, C.D., Jensen, E.L.N., *et al.*: Vetting of 384 TESS

objects of interest with TRICERATOPS and statistical validation of 12 planet candidates. Astron. J. **161**(1), 24 (2021) https://doi.org/10.3847/1538-3881/abc6af

[28] Collier, M., Giacalone, S., Derfer, B., Ciardi, D.R., *et al.*: Assessing the impact of high-resolution imaging on statistical validation of TESS planet candidates. Astron. J. **172**, 247 (2026) 2608.21560

[29] Bryson, S.T., Jenkins, J.M., Gilliland, R.L., *et al.*: Identification of background false positives from Kepler data. Publ. Astron. Soc. Pac. **125**(930), 889 (2013) https://doi.org/10.1086/671767

[30] Scott, N.J., Howell, S.B., Gnilka, C.L., *et al.*: Twin high-resolution, high-speed imagers for the Gemini telescopes: Instrument description and science verification results. Frontiers in Astronomy and Space Sciences **8**, 138 (2021) https://doi.org/10.3389/fspas.2021.716560

[31] Lindegren, L., Klioner, S.A., Hernández, J., *et al.*: Gaia early data release 3. the astrometric solution. Astron. Astrophys. **649**, 2 (2021) https://doi.org/10.1051/0004-6361/202039709

[32] Ioffe, S., Szegedy, C.: Batch normalization: Accelerating deep network training by reducing internal covariate shift. In: Proceedings of the 32nd International Conference on Machine Learning. PMLR, vol. 37, pp. 448–456 (2015)

[33] Srivastava, N., Hinton, G., Krizhevsky, A., Sutskever, I., Salakhutdinov, R.: Dropout: A simple way to prevent neural networks from overfitting. Journal of Machine Learning Research **15**(56), 1929–1958 (2014)

[34] Zucker, S., Giryes, R.: Shallow transits—deep learning. I. feasibility study of deep learning to detect periodic transits of exoplanets. Astron. J. **155**(4), 147 (2018) https://doi.org/10.3847/1538-3881/aaae05

[35] Prša, A., Kochoska, A., Conroy, K.E., *et al.*: TESS eclipsing binary stars. I. short-cadence observations of 4584 eclipsing binaries in sectors 1–26. Astrophys. J. Suppl. Ser. **258**(1), 16 (2022) https://doi.org/10.3847/1538-4365/ac324a

[36] Espinoza, N., Brahm, R., Henning, T., Jordán, A., *et al.*: HD 213885b: a transiting 1-d-period super-earth with an earth-like composition around a bright (V = 7.9) star unveiled by TESS. Mon. Not. R. Astron. Soc. **491**(2), 2982–2999 (2020) https://doi.org/10.1093/mnras/stz3150

[37] Guerrero, N.M., Seager, S., Huang, C.X., *et al.*: The TESS objects of interest catalog from the TESS prime mission. Astrophys. J. Suppl. Ser. **254**(2), 39 (2021) https://doi.org/10.3847/1538-4365/abefe1

[38] Jenkins, J.M., Twicken, J.D., McCauliff, S., *et al.*: The TESS science processing

operations center. In: Software and Cyberinfrastructure for Astronomy IV. Proc. SPIE, vol. 9913, p. 99133 (2016). https://doi.org/10.1117/12.2233418

[39] Huang, C.X., Vanderburg, A., Pál, A., *et al.*: Photometry of 10 million stars from the first two years of TESS full frame images: Part i. Res. Notes AAS **4**(11), 204 (2020)

[40] Pu, B., Lai, D.: Low-eccentricity migration of ultra-short-period planets in multiplanet systems. Mon. Not. R. Astron. Soc. **488**(3), 3568–3587 (2019)

[41] Lee, E.J., Chiang, E.: Magnetospheric truncation, tidal inspiral, and the creation of short-period and ultra-short-period planets. Astrophys. J. **842**(1), 40 (2017) https://doi.org/10.3847/1538-4357/aa6fb3

[42] Millholland, S.C., Spalding, C.: Formation of ultra-short-period planets by obliquity-driven tidal runaway. Astrophys. J. **905**(1), 71 (2020)

[43] Smith, J.C., Stumpe, M.C., Van Cleve, J.E., *et al.*: Kepler presearch data conditioning II—a Bayesian approach to systematic error correction. Publ. Astron. Soc. Pac. **124**(919), 1000 (2012)

[44] Stumpe, M.C., Smith, J.C., Van Cleve, J.E., *et al.*: Kepler presearch data conditioning I—architecture and algorithms for error correction in Kepler light curves. Publ. Astron. Soc. Pac. **124**(919), 985 (2012)

[45] Lightkurve Collaboration, Cardoso, J.V.d.M., Hedges, C., et al.: Lightkurve: Kepler and TESS time series analysis in Python. Astrophysics Source Code Library, ascl:1812.013 (2018)

[46] Domínguez Sánchez, H., Huertas-Company, M., Bernardi, M., Kaviraj, S., Fischer, J.L., *et al.*: Transfer learning for galaxy morphology from one survey to another. Mon. Not. R. Astron. Soc. **484**(1), 93–100 (2019) https://doi.org/10.1093/mnras/sty3497

[47] Pérez-Carrasco, M., Cabrera-Vives, G., Martinez-Marin, M., et al.: Multiband galaxy morphologies for CLASH: a convolutional neural network transferred from CANDELS. Publ. Astron. Soc. Pac. (2019) 1810.07857

[48] Tang, H., Scaife, A.M.M., Leahy, J.P.: Transfer learning for radio galaxy classification. Mon. Not. R. Astron. Soc. **488**(3), 3358–3375 (2019) https://doi.org/10.1093/mnras/stz1883

[49] Walmsley, M., Scaife, A.M.M., Lintott, C., *et al.*: Practical galaxy morphology tools from deep supervised representation learning. Mon. Not. R. Astron. Soc. **513**(2), 1581–1599 (2022) https://doi.org/10.1093/mnras/stac525

[50] Kingma, D.P., Ba, J.: Adam: A method for stochastic optimization. In: 3rd International Conference on Learning Representations (ICLR 2015), San Diego, CA (2015)

[51] Varma, S., Simon, R.: Bias in error estimation when using cross-validation for model selection. BMC Bioinformatics **7**, 91 (2006) https://doi.org/10.1186/1471-2105-7-91

[52] Cawley, G.C., Talbot, N.L.C.: On over-fitting in model selection and subsequent selection bias in performance evaluation. Journal of Machine Learning Research **11**(70), 2079–2107 (2010)

[53] Hanley, J.A., McNeil, B.J.: The meaning and use of the area under a receiver operating characteristic (ROC) curve. Radiology **143**(1), 29–36 (1982) https://doi.org/10.1148/radiology.143.1.7063747

[54] Narita, N., Fukui, A., Kusakabe, N., *et al.*: MuSCAT2: four-color simultaneous camera for the 1.52-m Telescopio Carlos Sánchez. Journal of Astronomical Telescopes, Instruments, and Systems **5**(1), 015001 (2019) https://doi.org/10.1117/1.JATIS.5.1.015001

[55] Parviainen, H., *et al.*: MuSCAT2 multicolour validation of TESS candidates: an ultra-short-period substellar object around an M dwarf. Astron. Astrophys. **633**, 28 (2020)

[56] Nutzman, P., Charbonneau, D.: Design considerations for a ground-based transit search for habitable planets orbiting M dwarfs. Publ. Astron. Soc. Pac. **120**(865), 317–327 (2008) https://doi.org/10.1086/533420

[57] Penoyre, Z., Belokurov, V., Evans, N.W.: Astrometric identification of nearby binary stars – II. astrometric binaries in the Gaia catalogue of nearby stars. Mon. Not. R. Astron. Soc. **513**(4), 5270 (2022) https://doi.org/10.1093/mnras/stac1079

[58] Chen, J., Kipping, D.: Probabilistic forecasting of the masses and radii of other worlds. Astrophys. J. **834**(1), 17 (2017) https://doi.org/10.3847/1538-4357/834/1/17

[59] Espinoza, N., Kossakowski, D., Brahm, R.: juliet: a versatile modelling tool for transiting and non-transiting exoplanetary systems. Mon. Not. R. Astron. Soc. **490**(2), 2262–2283 (2019) https://doi.org/10.1093/mnras/stz2688

[60] Kreidberg, L.: batman: BAsic Transit Model cAlculatioN in Python. Publ. Astron. Soc. Pac. **127**(957), 1161 (2015) https://doi.org/10.1086/683602

[61] Speagle, J.S.: dynesty: a dynamic nested sampling package for estimating Bayesian posteriors and evidences. Mon. Not. R. Astron. Soc. **493**(3), 3132–3158

(2020) https://doi.org/10.1093/mnras/staa278

[62] Kipping, D.M.: Efficient, uninformative sampling of limb darkening coefficients for two-parameter laws. Mon. Not. R. Astron. Soc. **435**(3), 2152–2160 (2013) https://doi.org/10.1093/mnras/stt1435

[63] Goldreich, P., Soter, S.: Q in the solar system. Icarus **5**, 375–389 (1966) https://doi.org/10.1016/0019-1035(66)90051-0

[64] Hamer, J.H., Schlaufman, K.C.: Ultra-short-period planets are stable against tidal inspiral. Astron. J. **160**(3), 138 (2020) https://doi.org/10.3847/1538-3881/ab9b27

[65] López-Morales, M., Seager, S.: Thermal emission from transiting very hot jupiters: Prospects for ground-based detection of secondary eclipses. Astrophys. J. Lett. **667**(2), 191 (2007)

[66] Elkins-Tanton, L.T.: Magma oceans in the inner solar system. Annual Review of Earth and Planetary Sciences **40**, 113–139 (2012)

[67] Kempton, E.M.-R., Bean, J.L., Louie, D.R., *et al.*: A framework for prioritizing the TESS planetary candidates most amenable to atmospheric characterization. Publ. Astron. Soc. Pac. **130**(993), 114401 (2018) https://doi.org/10.1088/1538-3873/aadf6f

[68] Smith, A.M.S., Cáceres, C., Csizmadia, S., *et al.*: K2-137 b: an earth-sized planet in a 4.3-h orbit around an M-dwarf. Mon. Not. R. Astron. Soc. **474**(4), 5523–5533 (2018) https://doi.org/10.1093/mnras/stx2891

[69] Dai, F., et al.: TOI-6255 b: An earth-sized planet on the verge of tidal disruption. Astron. J. (2024)

[70] Lee, E.J., et al.: TOI-6324 b: An earth-mass ultra-short-period planet transiting a nearby M dwarf. Astron. J. (2025)

[71] Gomez Barrientos, J., Greklek-McKeon, M., Knutson, H.A., *et al.*: Validation of TESS planet candidates with multicolor transit photometry and TRICERATOPS+. Astron. J. (2025) https://doi.org/10.3847/1538-3881/ade68b 2508.02782